ARTICLES
https://doi.org/10.1038/s41563-021-01185-y

nature materials

Universal scaling law of glass rheology

Shuangxi Song[1], Fan Zhu[1,2,4] and Mingwei Chen[2,3]✉

The similarity in atomic/molecular structure between liquids and glasses has stimulated a long-standing hypothesis that the nature of glasses may be more fluid-like, rather than the apparent solid. In principle, the nature of glasses can be characterized by the dynamic response of their rheology in a wide rate range, but this has not been realized experimentally, to the best of our knowledge. Here we report the dynamic response of shear stress to the shear strain rate of metallic glasses over a timescale of nine orders of magnitude, equivalent to hundreds of years, by broadband stress relaxation experiments. The dynamic response of the metallic glasses, together with other 'glasses', follows a universal scaling law within the framework of fluid dynamics. The universal scaling law provides comprehensive validation of the conjecture on the jamming (dynamic) phase diagram by which the dynamic behaviours of a wide variety of 'glasses' can be unified under one rubric parameterized by the thermodynamic variables of temperature, volume and stress in the trajectory space.

It has been well established that plastic flow of crystalline materials is predominantly conducted by the formation and/or motion of discrete crystal defects such as vacancies, dislocations, stacking faults, twins and grain boundaries in various stress, time and temperature domains[1]. By contrast, simple and complex liquids behave in a viscous or viscoelastic fashion. Unlike crystals and liquids, glasses such as metallic glasses (MGs) and window (silicate) glasses usually have liquid-like disordered atomic/molecular structures but are stiff and hard as brittle solids. Owing to the similarity in atomic structure between liquids and glasses, it has been long conjectured that glasses may retain the nature of liquids[2–5], as indicated by some peculiar glass flowing observations from the thickened bottoms of stained glass panes in old European churches[6]. Physically, the nature of glasses can be characterized by correlating the dynamic response of plastic flow to applied force in a wide time range. However, in the accessible timescale of conventional mechanical testing techniques, glasses usually behave as the elastoplastic materials with trivial temperature and strain-rate sensitivity. As a result, comprehensive assessments of the dynamic behaviour of glasses have not been realized by direct experimental measurements or Williams–Landel–Ferry time–temperature superposition function analysis in the glass state[7]. Under quasi-static loading conditions, the plastic rheology of glasses is usually associated with the collection of local shearing events, most likely from small-scale structure and density fluctuations[8,9]. For MGs, the local shearing is described by a dynamic variable, the shear transformation zone (STZ), which represents the evolution of shear-induced local atomic configurations[10–15]. The experimentally accessible parameter, which can microscopically depict the plastic flow of MGs, is the statistical size of STZs. Depending on theoretical models and experimental methods, estimated STZ volumes have been reported to vary over two orders of magnitude from several atoms to hundreds of atoms[16–19], which is far beyond possible experimental error. In fact, the large discrepancy in the STZ volumes has caused intense debate and confusion on the understanding of rheology mechanisms in MGs. We noticed that previous experiments were carried out within a limited strain-rate range in different time domains. The dispute over rheology behaviour may arise from a distinct rate/time dependence of flow mechanisms, although the mechanical behaviour of MGs is usually considered time insensitive at temperatures far below the glass transition point (T_g). Thus, to have a thorough understanding on the rheology and thus the nature of the hard glasses, it is necessary to design and carry out experiments that are capable of measuring the dynamic response of MGs over a broad strain-rate range.

As shown in Fig. 1a we measured the dynamic shear stress response of a $Zr_{55}Cu_{30}Al_{10}Ni_5$ MG at shear strain rates ranging from 10^{-8} to $10^{0}\,s^{-1}$ by combining broadband nanoindentation and cantilever bending methods at room temperature. In the stress relaxation experiments, shear strain rate ($\dot{\gamma}$) and nominal shear stress (τ) are derived from the contact force (P) and displacement (h) at different relaxation times (t; Methods). The estimated shear stress is plotted as the function of shear strain rate for the high-rate nanoindentation (Fig. 1b) and low-rate cantilever experiments (Fig. 1c). The stress relaxation experiments at low stress levels are essentially creep testing. The small sampling volumes required by nanoindentation and cantilever experiments effectively avoid the interference of discrete shear banding and cracking at high stress levels. The experimental data points obtained by the two different methods perfectly overlap with each other in the strain rate range between ~10^{-6} and $10^{-5}\,s^{-1}$ and form one smooth curve (Fig. 2a). Therefore, the dynamic mechanical response of a material in the glass state is presented successfully over the wide rate range from ~10^{-8} to $10^{0}\,s^{-1}$, a timescale spanning nine orders of magnitude. In comparison with the conventional high-temperature dynamic mechanical analysis, by which a wide time range of elastic and viscoelastic response can be obtained by time–temperature superposition[20], the broadband stress relaxation experiments allow us to directly measure the stress–strain responses at a temperature far below T_g and a stress below and above the yield point. The capability of low temperature and high stress measurements is essential for illustrating the full-spectrum dynamic response of the glass state as shown in Fig. 2a. Converting the stress–strain relation into a log–log plot gives two distinct linear regions with two dramatically different slopes, that is, strain rate sensitivities ($m = \partial \ln \tau / \partial \ln \dot{\gamma}$), at high and low strain rates (stresses). At high strain rates (>$10^{-4}\,s^{-1}$), the experimental data can be well fitted by the Johnson–Samwer cooperative shear

[1]State Key Laboratory of Metal Matrix Composites, School of Materials Science and Engineering, Shanghai Jiao Tong University, Shanghai, PR China. [2]WPI Advanced Institute for Materials Research, Tohoku University, Sendai, Japan. [3]Department of Materials Science and Engineering, Hopkins Extreme Materials Institute, Johns Hopkins University, Baltimore, MD, USA. [4]Present address: Department of Materials Science, Fudan University, Shanghai, China. ✉e-mail: mwchen@jhu.edu

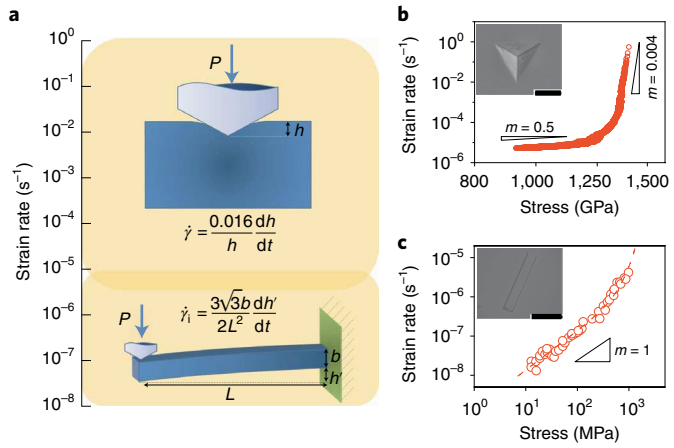

Fig. 1 | Broadband relaxation experiments of a $Zr_{55}Cu_{30}Al_{10}Ni_5$ glass. **a**, Schematic drawing of broadband stress relaxation experiments by using nanoindentation (above) and cantilever bending (bottom) tests with a total measurable strain rate range from 10^{-8} to 10^{0} s^{-1}. *L*, distance between the clamp and indenter tip contact point; *b*, sample thickness; *h*′, bending displacement; $\dot{\gamma}_i$, time derivative of γ_i. **b**,**c**, Shear strain rate as a function of shear stress calculated from nanoindentation relaxation measurements (**b**) and cantilever bending relaxation measurements (**c**). Scanning electron microscopy images of an indent after a nanoindentation relaxation test at 10 mN for 2,000 s with a scale bar of 1 μm and a typical cantilever with a scale bar of 100 μm are inserted in **b** and **c**, respectively. Rate sensitivity (*m*) of 1, 0.5 and 0.004 is plotted as a triangle slope to guide the eye.

model (CSM) portrayed by a sinusoidal function of megabasin potential energy density[12]:

$$\dot{\gamma} = \dot{\gamma}_0 \exp\left(-\frac{W_{CSM}}{kT}\right) \quad (1)$$

where $\dot{\gamma}_0 \approx 10^{10}$ s^{-1} is the elastic strain rate limit[12]; W_{CSM} is the activation energy of cooperative shear, which depends on stress (Methods); *k* is the Boltzmann constant; and *T* is temperature. On the other hand, at strain rates below 10^{-6} s^{-1}, the flow rate follows a power law with a rate sensitivity or power index of unity. In this case, the rate–stress dependence can be described by the reversible STZ-free volume model originally derived from the transition state theory by Spaepen and Argon[10,11]:

$$\dot{\gamma} = \alpha\gamma_0\nu_G \exp\left(-\frac{W_{STZ}}{kT}\right)\sinh\left(\frac{\tau\gamma_0\Omega}{2kT}\right) \quad (2)$$

where α (of order unity) is the steady-state volume fraction of flow units contributing to plastic flow; γ_0 represents the transformation strain of STZs and is taken as 0.125; $\nu_G \approx 10^{13}$ s^{-1} is the intrinsic phonon relaxation time[21]; and W_{STZ} and Ω are the activation energy and volume of STZs[10]. The activation energy and size of STZs by fitting the strain rate data in Figs. 1b,c and 2a using equations (1) and (2) are listed in Supplementary Table 1. The STZ size at high stresses is determined to be ~5.64 nm^3 or 338 atoms by CSM, consistent with previously reported rate-jump measurements of Zr-based MGs at high stresses and strain rates[17]. The activation energy for the cooperative shear is estimated to be 5.91 eV, close to that for the α relaxation[22]. By contrast, the STZ volume at low stresses is measured to be only ~0.22 nm^3 or 16 atoms, in agreement with previous relaxation spectrum measurements[16] as well as those measurements at temperatures close to T_g (ref. [19]). Correspondingly, a low activation energy of only ~1.08 eV and small activation volume (V^*) of 0.028 nm^3 or a single atom by $V^* = \gamma_0\Omega$ are obtained from the transition state theory equation. Both the activation volume and activation energy indicate that dynamic flow of the MG at low strain rates can be described by single-atom motion or synchronized motion of all atoms at the same pace. In particular, the linear correlation between shear stress and shear strain rate at rates below 10^{-7} s^{-1} indicates that the MG follows the behaviour of a Newtonian flow at low rates.

In the transition region, the strain rate sensitivity drops sharply from ~1.0 to 0.004 within a narrow strain rate range between 10^{-6} and 10^{-4} s^{-1} (inset in Fig. 2a). This suggests a dynamic transition from viscoelastic to elastoplastic deformation with substantial increases in flow stress, activation energy and STZ volume. We noticed that the dynamic transition includes two distinct stages: from Newtonian to non-Newtonian and from non-Newtonian to cooperative shear, as marked by the arrows in Supplementary Fig. 1a. Although the Johnson–Samwer CSM model[23] and Langer–Falk STZ model[12] predict the Newtonian to non-Newtonian and/or the non-Newtonian to cooperative shear transitions, there is obvious divergence between the broadband experimental data and these models (Supplementary Fig. 1a and Supplementary Fig. 7). In fact, we found that the experimental data in the transition region can be best fitted by the Kohlrausch (or stretched exponential) relaxation function as shown by the black line in Fig. 2a and Supplementary Fig. 1. This indicates that the dynamic response in the transition region may involve many-body interactions[24,25], most likely related to the thermal and athermal coalescence of STZs, flow units[20] or shear microdomains[26]. This greatly contrasts the CSM and STZ models[8–10,12] as they essentially describe a single-body process.

On the basis of the shear stress and shear strain rate measurements in Fig. 2a, the viscosity ($\eta = \tau/\dot{\gamma}$) of the MG is calculated and plotted as the function of strain rate in Supplementary Fig. 2. The Newtonian viscosity (η_N) of the MG is estimated to be ~8.5×10^{14} Pa s at room temperature. The viscosity of the MG at room temperature and the literature data of other Zr-based MGs achieved at high temperatures near T_g (ref. [27]) are plotted in Supplementary Fig. 3a. The viscosity data are normalized by the Newtonian viscosity at each temperature and plotted as a function of strain rate in Supplementary Fig. 3b. The relationship between normalized viscosity (η/η_N) and the strain rate of all data shows the same trend from Newtonian flow at low strain rates to shear thinning at high strain rates. These observations are in good agreement with previous viscosity measurements and simulations of glass-forming liquids[23,27–29]. The normalized viscosities of MGs are plotted as a function of the scaled shear strain rate ($\dot{\gamma}\eta_N$), that is, viscous stress in Newtonian flow (Fig. 2b), which includes the data from the current broadband experiments and the literature data from high-temperature deformation, room-temperature creep and dynamic mechanical analysis of Zr-based and La-based MGs[27,30–33]. It is immediately evident that all the data approximately fall on one master curve that spans a wide shear strain rate regime from 10^{-9} to 10^{6} s^{-1}, independent of temperature (below or above T_g; that is, in a glass or liquid state), chemical composition and sample geometry.

We noticed that the similar dynamic trend of normalized viscosity as the function of scaled strain rate can be obtained from a wide range of 'glass' systems, including inorganic glasses[34], polymer glasses[35–37], emulsifiers[38], granular materials[39], soil liquefaction[40] and even fire ant aggregations[41] (Fig. 2c). However, the viscous stresses (that is, $\dot{\gamma}\eta_N$) of these 'glass' systems vary by several orders of magnitude. Based on the scaling law for the yield strength of glasses, $\tau_C = 3k(T_g - T)/V$, acquired in our previous study[42], the normalized viscosity is further plotted as the function of a dimensionless parameter $\dot{\gamma}\eta_N\frac{V}{3kT_g}$ in Fig. 2d, where *V* is the average molar volume determined from average atomic or particulate weight *M* and density ρ, that is, $V = M/\rho$ (Supplementary Table 2). It is remarkable that the experimental data from all 'glass' systems fall within close proximity to the one master curve in Fig. 2d, demonstrating that

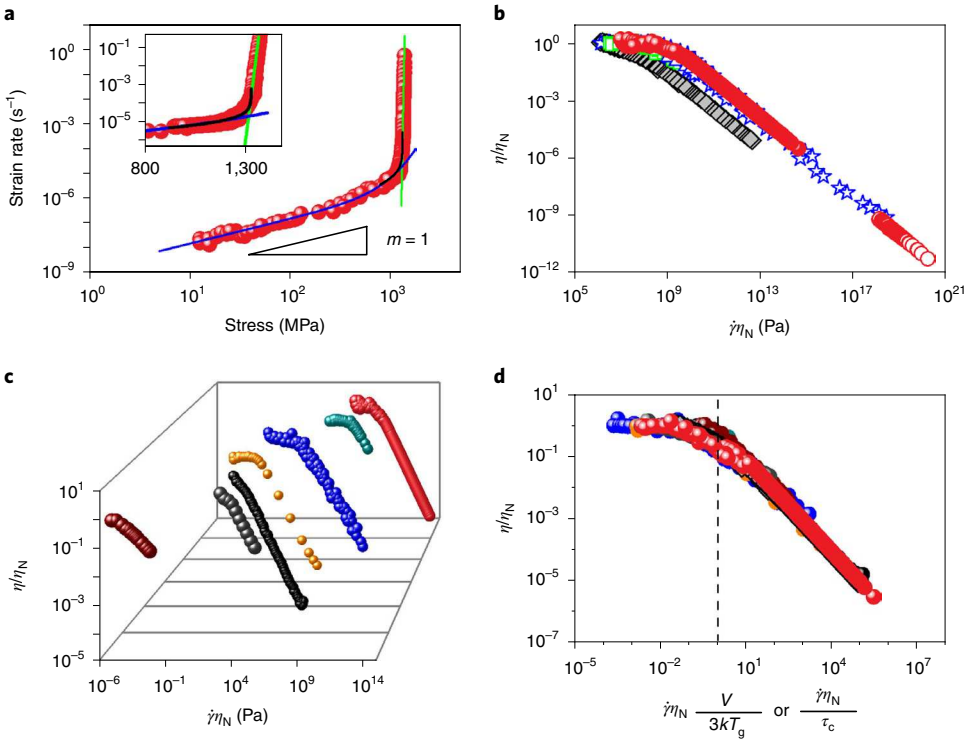

Fig. 2 | Strain-rate/stress behaviour and universal scaling law of glass rheology. a, The logarithmic plot of the shear strain rate as a function of shear stress for the $Zr_{55}Cu_{30}Al_{10}Ni_5$ glass under nanoindentation and cantilever bending at room temperature. Rate sensitivity (m) of 1 is plotted as a triangle slope to guide the eye. The inset is the enlarged view of the transition segment together with the fitting curves based on the transition state theory (blue line), the cooperative shear model (green line) and the Kohlrausch relaxation equation (black line). **b**, Normalized viscosity as a function of scaled strain rate by Newtonian viscosity from the broadband relaxation measurements at room temperature (red balls); dynamic mechanical analysis relaxation measurements of $La_{60}Ni_{15}Al_{25}$ MG at various temperatures with 0.005 initial strain (grey diamonds)[20]; and creep data from compression at room temperature (blue open triangles)[31,33] and 613–683 K (green open squares) in Vitreloy 1 glass[27], together with molecular dynamics simulation results in a Cu–Zr glass (blue pentacles)[30] and viscosity measured for propagating shear bands in a Zr-based MG at room temperature (open red circles)[32]. **c**, Normalized viscosity as a function of strain rate scaled by Newtonian viscosity from various 'glass' materials. MG data are plotted as red balls. Silicate glass non-Newtonian flow data are plotted as dark cyan balls[34]. Viscosity data of polyethylene[36], polypropylene[35] and polybutadiene rubber[37] are plotted as blue balls. The ant aggregation viscous data are plotted as black balls[41]. Mayonnaise non-Newtonian flow data are plotted as orange balls[38]. Granular[39] and soil[40] data are plotted as dark grey and wine balls, respectively. **d**, Normalized viscosity as a function of dimensionless quantities as $\dot{\gamma}\eta_N \frac{V}{3kT_g}$ or $\frac{\dot{\gamma}\eta_N}{\tau_C}$ in various 'glass' materials; the dashed line at $\dot{\gamma}\eta_N \frac{V}{3kT_g} = 1$ is for guidance.

the dynamic response of the 'glass' systems can be described by a universal scaling law. Remarkably, the rheology of a wide variety of disordered systems is unified by a single scaling law. Note that $\dot{\gamma}\eta_N \frac{V}{3kT_g}$ is equivalent to $\frac{\dot{\gamma}\eta_N}{\tau_C} = B_i$, where B_i is the Bingham number defined as the ratio of the viscous stress ($\dot{\gamma}\eta_N$) of liquids to the elastic shear stress limit (that is, yield strength) τ_C at $T = 0$ K with a molar volume V (ref. [43]). Therefore, the universal scaling law that is derived to describe the dynamic response of the 'glass' systems is, in fact, within the framework of the classical fluid dynamics.

The scaled rheological behaviour exhibits two linear regimes with distinct slopes in the double-log plot (Fig. 2d). The slope is zero in the low-rate Newtonian flow region, suggesting a rate-independent property of equilibrium liquids. By contrast, in the high-flow-rate or high-viscous-stress region, the slope gradually approaches −1. Similar to the ideal steady flow of polymeric liquids at high strain rates[44], the negative unit slope in the non-Newtonian regime indicates that the nominal shear stresses of the elastoplastic behaviour reach a maximum and the plastic flow is dominated by an athermal process. It is evident that, if the applied stress or strain rate is below a critical value, that is, $\dot{\gamma}\eta_N \frac{V}{3kT_g} < 1$, the 'glass' systems show a liquid behaviour and the rheology is dominated by thermally activated Newtonian flow (Fig. 2d). However, when $\dot{\gamma}\eta_N \frac{V}{3kT_g} > 1$, the systems become solid-like and the rheology is mainly controlled by stress-driven cooperative shear, which manifests as the coalescence of STZs in MGs. Conventionally, this yielding or shear thinning process is considered as the onset of time-independent elastoplastic flow in glass materials or unjamming in granular materials as the transient plastic flow is readily noticed. In other words, the universal scaling law reveals a mechanistic transition from thermally activated Newtonian flow to stress-driven cooperative shear which takes place when

$$\dot{\gamma}\eta_N \frac{V}{3kT_g} = 1. \quad (3)$$

Therefore, the transition between liquid and glass essentially depends on four parameters: molar volume V or density; temperature, T; experimental or observation time, $\dot{\gamma}$ or t_{obs}; and stress, τ. In principle, the transition can be defined by one of the four variables and described by a three-dimensional (3D) contoured surface in temperature–stress–volume, temperature–stress–time, temperature–time–volume or time–volume–stress phase spaces. For example, in a typical case of time being the critical variable[30,45–47], the transition can be presented on a 3D contoured surface in the temperature–stress–volume space with three scaled variables of kT/U_0, τ/τ_0 and V/V_0 as the axes (Fig. 3a). Here, $U_0 = 3kT_g$ is the thermal energy required for glass transition at zero stress and the maximum density[42], τ_0 is the critical strength at 0 K and the maximum

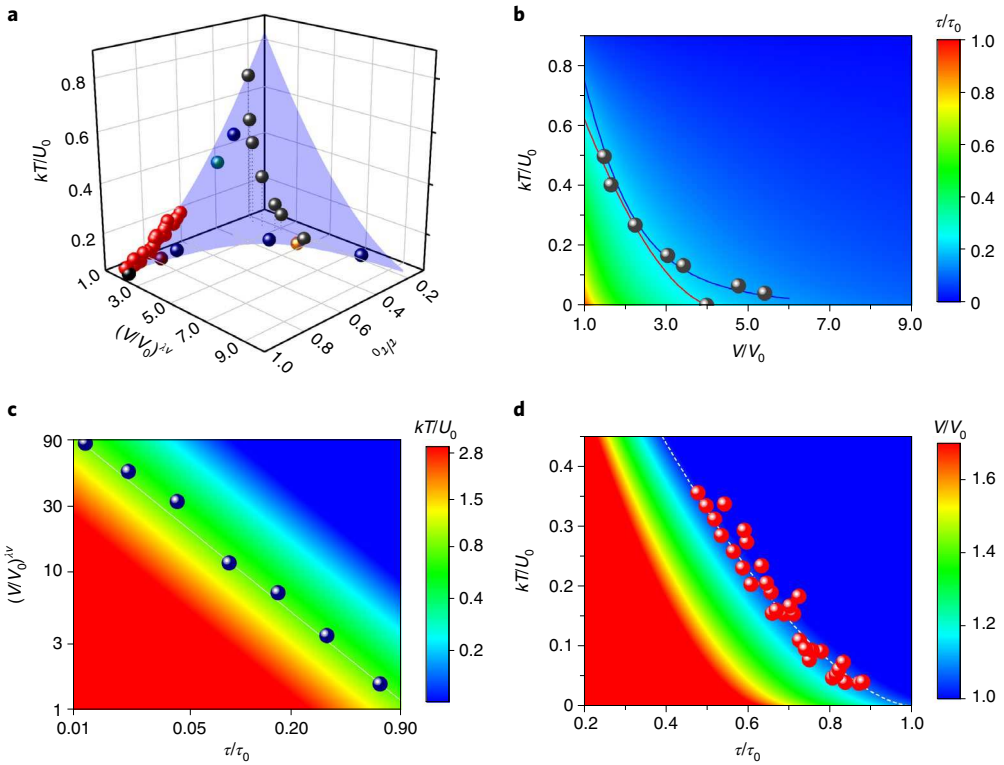

Fig. 3 | Dynamic transition phase diagram based on the universal law derived from the broadband relaxation measurements. a, Perspective view of the transition boundary diagram plotted as a transparent blue surface with three orthogonal axes of normalized stress τ/τ_0, normalized molar volume $(V/V_0)^{\lambda_V}$ and reduced temperature kT/U_0 following equations (3) and (S15) when $\lambda_V=1$. The temperature dependence on τ/τ_0 and V/V_0 for various MGs in ref. [12] and this study is plotted as red balls that coincide on the boundary surface in the MG region. The jamming transition boundary values for attractive particles from the literature at $U_0\approx 20kT$ (ref. [46]) and for granular materials[49] are plotted as navy balls and dark grey balls, respectively. The transition points of the 'glass' materials from Fig. 2c are also plotted with the same colour scheme. **b**, Phase diagram of two control parameters, kT/U_0 and V/V_0, in a granular system with a constant driving force. **c**, Two-dimensional boundary log–log plot of V/V_0 as a function of τ/τ_0 at $U_0\approx 20kT$ for attractive polystyrene particles; the molar volume is normalized with $(V/V_0)^{\lambda_V}$ with $\lambda_V=3.2$. **d**, Two-dimensional boundary plot of kT/U_0 as a function of τ/τ_0 at constant V/V_0 for MGs. See Supplementary Information for details on curve fitting.

density, and V_0 is the molar volume at 0 K and at zero stress. The transition boundary can be determined by critical-like equations where the three scaled variables are correlated[46,48] (Supplementary Information). Experimental data of the transition for metallic glasses, plotted as red solid spheres in Fig. 3a, are located at the transition boundary[12], together with the literature data from a granular system under a constant driving force or tapping (shown as dark grey spheres)[49] and the attractive particles with $U_0\approx 20kT$ (shown as navy spheres[46] in Fig. 3a). The transition points from the master curves in Fig. 2d are also plotted in Fig. 3a. The glass systems are in an equilibrium and reversible state underneath the contoured boundary but become off-equilibrium and irreversible above the boundary.

In practice, one of the three thermodynamic variables often keeps constant or approximately unchanged during experiments, and thereby the transition can be determined by a planar cut of the 3D contour. For example, under a constant driving force, the transition boundary in the granular system from the reversible to irreversible regimes by jamming and unjamming can be plotted as a contour curve in the two-dimensional domain of configurational temperature (or tapping amplitude) and molar volume (or density) in Fig. 3b. For the attractive particles at a constant temperature, the transition boundary is a contour curve in the V/V_0 (or $(V/V_0)^{\lambda_V}$) and τ/τ_0 domain in Fig. 3c. The exponential dependence with coefficient λ_V is related to the formation of attractive particle clusters, and the density of a fractal aggregate decreases as the cluster grows[46]. In the case of MGs, the density change is negligible and the transition is presented well in the temperature–stress domain in Fig. 3d. When the stress is small or remains nearly constant in conventional viscosity measurements, the dynamic transition is presented as the correlation between time and temperature, similar to the observed crossover from Arrhenius to non-Arrhenius liquids[50,51]. For our broadband stress relaxation measurements, the temperature and volume are nearly constant. Thus, the rheological behaviour degenerates to the correlation between time (strain rate) and shear stress. As a result, the transition can be conveniently described by either correlated time (strain rate) or stress[30,42].

Liu and Nagel[45] have proposed a conjecture that the dynamic transitions in a variety of disordered systems, such as the jamming–unjamming transition in granular materials and foams and the liquid-to-glass transition in glass-forming materials, can be brought together under one rubric and unified by a 3D jamming phase diagram parameterized by thermodynamic variables of temperature, density (volume) and force. In the past decade, this hypothesis has been partially confirmed by computer simulations and experiments in granular and glass systems[30,46,47,52]. However, a comprehensive validation has not been achieved. Our universal scaling law, derived from the dynamic responses of a broad range of 'glass' systems, provides theoretical confirmation of the hypothesis. The resulting phase diagram in the temperature–stress–volume space (Fig. 3), identical to the concept of a jamming phase diagram, can quantitatively represent the experimental observations on the temperature- and volume-controlled jamming transition of a granular system with a constant driving force, a stress- and

volume-controlled jamming transition in attractive particles and a temperature- and stress-controlled glass transition in glass-forming materials. Importantly, the unified phase diagram from the universal scaling law unveils the dynamic nature of 'glass' systems in the framework of the classical fluid dynamics; that is, the jamming and glass transitions occur in the trajectory space (space–time) rather than in the configuration space and, therefore, are controlled by thermodynamic variables of stress (pressure), volume (density) and temperature that drive the systems out of equilibrium[53]. In fact, the 'glass' systems are ergodic when they are in the equilibrium Newtonian flow region. When the system is out of equilibrium above the phase boundary, it is nonergodic and the motions of the constituent particles become correlated throughout the observation time. The boundary for the transition where the ergodic and nonergodic phases are separated by a critical temporal variable can thus be described by a contoured surface of the three thermodynamic parameters of stress (pressure), volume (density) and temperature by the universal scaling law and the dynamic (jamming) phase diagram.

Besides the scientific importance of the universal scaling law in unveiling the nature of 'glasses' and in describing the dynamic transitions of 'glass' systems, the scaling law also provides important guidance for designing and employing 'glass' materials for practical applications. For example, the equal role of temperature and stress in the glass transition directs the alloy design of high-temperature MGs by considering strong and refractory elements[54], and warrants attention on the thermal and mechanical stability of glasses as a force-bearing component serving at temperatures even below calorimetric T_g, a temperature that is conventionally determined by differential scanning calorimetry at zero force. For granular materials, the universal scaling law may bring new insights and attentions to the possible effect of configurational temperature, in addition to the known pressure and density, on landslides and riverbank collapses by soil liquefaction[55].

In summary, the broadband dynamic response of MGs, together with a wide variety of other 'glass' systems, can be unified by a universal scaling law within the framework of the classical fluid dynamics. The scaling law provides comprehensive validation of the conjecture of the dynamic (jamming) phase diagram and demonstrates that the dynamic transition of disordered systems can be described by the conversion between equilibrium Newtonian liquids and off-equilibrium elastoplastic solids. This work uncovers the liquid nature of glasses and offers a quantitative description of the dynamic transition of 'glass' systems by the thermodynamic variables of temperature, volume and stress in the trajectory space.

Online content

Any methods, additional references, Nature Research reporting summaries, source data, extended data, supplementary information, acknowledgements, peer review information; details of author contributions and competing interests; and statements of data and code availability are available at https://doi.org/10.1038/s41563-021-01185-y.

Received: 13 September 2020; Accepted: 8 December 2021;
Published online: 31 January 2022

References

1. Frost, H. J. & Ashby, M. F. *Deformation-Mechanicsm Maps: the Plasticity and Creep of Metals and Ceramics* 165 (Pergamon Press, 1982).
2. Anderson, P. W. Through the glass lightly. *Science* **267**, 1615–1616 (1995).
3. Langer, J. The mysterious glass transition. *Phys. Today* **60**, 8 (2007).
4. Ediger, M. D. & Harrowell, P. Perspective: supercooled liquids and glasses. *J. Chem. Phys.* **137**, 080901 (2012).
5. Wang, W. H. Dynamic relaxations and relaxation-property relationships in metallic glasses. *Prog. Mater. Sci.* **106**, 100561 (2019).
6. Chang, K. The nature of glass remains anything but clear. *The New York Times* https://www.nytimes.com/2008/07/29/science/29glass.html (29 July 2008).
7. Williams, M. L., Landel, R. F. & Ferry, J. D. The temperature dependence of relaxation mechanisms in amorphous polymers and other glass-forming liquids. *J. Am. Chem. Soc.* **77**, 3701–3707 (1955).
8. Zhu, F. et al. Correlation between local structure order and spatial heterogeneity in a metallic glass. *Phys. Rev. Lett.* **119**, 215501 (2017).
9. Huang, B. et al. Density fluctuations with fractal order in metallic glasses detected by synchrotron X-ray nano-computed tomography. *Acta Mater.* **155**, 69–79 (2018).
10. Argon, A. S. Plastic-deformation in metallic glasses. *Acta Metall.* **27**, 47–58 (1979).
11. Spaepen, F. A microscopic mechanism for steady-state inhomogeneous flow in metallic glasses. *Acta Metall.* **25**, 407–415 (1977).
12. Johnson, W. L. & Samwer, K. A universal criterion for plastic yielding of metallic glasses with a $(T/T_g)^{2/3}$ temperature dependence. *Phys. Rev. Lett.* **95**, 195501 (2005).
13. Chen, M. W. Mechanical behavior of metallic glasses: microscopic understanding of strength and ductility. *Ann. Rev. Mater. Res.* **38**, 445–469 (2008).
14. Falk, M. L., Langer, J. S. & Pechenik, L. Thermal effects in the shear-transformation-zone theory of amorphous plasticity: comparisons to metallic glass data. *Phys. Rev. E* **70**, 011507 (2004).
15. Hufnagel, T. C., Schuh, C. A. & Falk, M. L. Deformation of metallic glasses: recent developments in theory, simulations, and experiments. *Acta Mater.* **109**, 375–393 (2016).
16. Ju, J. D., Jang, D., Nwankpa, A. & Atzmon, M. An atomically quantized hierarchy of shear transformation zones in a metallic glass. *J. Appl. Phys.* **109**, 053522 (2011).
17. Pan, D., Inoue, A., Sakurai, T. & Chen, M. W. Experimental characterization of shear transformation zones for plastic flow of bulk metallic glasses. *Proc. Natl Acad. Sci. USA* **105**, 14769–14772 (2008).
18. Puthoff, J. B., Jakes, J. E., Cao, H. & Stone, D. S. Investigation of thermally activated deformation in amorphous PMMA and Zr-Cu-Al bulk metallic glasses with broadband nanoindentation creep. *J. Mater. Res.* **24**, 1279–1290 (2009).
19. Schuh, C. A., Hufnagel, T. C. & Ramamurty, U. Mechanical behavior of amorphous alloys. *Acta Mater.* **55**, 4067–4109 (2007).
20. Wang, Z., Sun, B. A., Bai, H. Y. & Wang, W. H. Evolution of hidden localized flow during glass-to-liquid transition in metallic glass. *Nat. Commun.* **5**, 5823 (2014).
21. Pietanza, L. D., Colonna, G., Longo, S. & Capitelli, M. Electron and phonon relaxation in metal films perturbed by a femtosecond laser pulse. *Appl. Phys. A* **79**, 1047–1050 (2004).
22. Qiao, J. C. & Pelletier, J. M. Dynamic mechanical analysis in La-based bulk metallic glasses: secondary (β) and main (α) relaxations. *J. Appl. Phys.* **112**, 083528 (2012).
23. Johnson, W. L., Demetriou, M. D., Harmon, J. S., Lind, M. L. & Samwer, K. Rheology and ultrasonic properties of metallic glass-forming liquids: a potential energy landscape perspective. *MRS Bull.* **32**, 644–650 (2007).
24. Angell, C. A. Perspective on the glass transition. *J. Phys. Chem. Solids* **49**, 863–871 (1988).
25. Ngai, K. L. *Relaxation and Diffusion in Complex Systems* (Springer, 2011).
26. Perez, J. Homogeneous flow and anelastic/plastic deformation of metallic glasses. *Acta Metall.* **32**, 2163–2173 (1984).
27. Lu, J., Ravichandran, G. & Johnson, W. L. Deformation behavior of the $Zr_{41.2}Ti_{13.8}Cu_{12.5}Ni_{10}Be_{22.5}$ bulk metallic glass over a wide range of strain-rates and temperatures. *Acta Mater.* **51**, 3429–3443 (2003).
28. Demetriou, M. D. et al. Cooperative shear model for the rheology of glass-forming metallic liquids. *Phys. Rev. Lett.* **97**, 065502 (2006).
29. Ingebrigtsen, T. S. & Tanaka, H. Structural predictor for nonlinear sheared dynamics in simple glass-forming liquids. *Proc. Natl Acad. Sci. USA* **115**, 87–92 (2018).
30. Guan, P., Chen, M. & Egami, T. Stress-temperature scaling for steady-state flow in metallic glasses. *Phys. Rev. Lett.* **104**, 205701 (2010).
31. Park, K.-W., Lee, C.-M., Kim, H.-J., Lee, J.-H. & Lee, J.-C. A methodology of enhancing the plasticity of amorphous alloys: elastostatic compression at room temperature. *Mater. Sci. Eng. A* **499**, 529–533 (2009).
32. Song, S. X. & Nieh, T. G. Direct measurements of shear band propagation in metallic glasses – an overview. *Intermetallics* **19**, 1968–1977 (2011).
33. Yoo, B.-G. et al. Increased time-dependent room temperature plasticity in metallic glass nanopillars and its size-dependency. *Int. J. Plast.* **37**, 108–118 (2012).
34. Brückner, R. & Yue, Y. Non-Newtonian flow behaviour of glass melts as a consequence of viscoelasticity and anisotropic flow. *J. Non-Cryst. Solids* **175**, 118–128 (1994).
35. Köpplmayr, T. et al. A novel online rheometer for elongational viscosity measurement of polymer melts. *Polym. Test.* **50**, 208–215 (2016).

36. Malkin, A. Y. Non-Newtonian viscosity in steady-state shear flows. *J. Non-Newton. Fluid Mech.* **192**, 48–65 (2013).
37. Roland, C. M. in *The Science and Technology of Rubber* 4th edn (eds Erman, B., Mark, J. E. & Roland, C. M.) Ch. 6 (Academic Press, 2013).
38. Mackley, M. R. et al. The observation and evaluation of extensional filament deformation and breakup profiles for non Newtonian fluids using a high strain rate double piston apparatus. *J. Non-Newton. Fluid Mech.* **239**, 13–27 (2017).
39. Olsson, P. & Teitel, S. Critical scaling of shear viscosity at the jamming transition. *Phys. Rev. Lett.* **99**, 178001 (2007).
40. Jeong, S. W., Locat, J., Leroueil, S. & Malet, J.-P. Rheological properties of fine-grained sediment: the roles of texture and mineralogy. *Can. Geotech. J.* **47**, 1085–1100 (2010).
41. Tennenbaum, M., Liu, Z., Hu, D. & Fernandez-Nieves, A. Mechanics of fire ant aggregations. *Nat. Mater.* **15**, 54–59 (2016).
42. Liu, Y. H. et al. Thermodynamic origins of shear band formation and the universal scaling law of metallic glass strength. *Phys. Rev. Lett.* **103**, 065504 (2009).
43. Bird, R. B., Dai, G. C. & Yarusso, B. J. The rheology and flow of viscoplastic materials. *Rev. Chem. Eng.* **1**, 1–70 (1983).
44. Doi, M. & Edwards, S. F. Dynamics of concentrated polymer systems. Part 4. Rheological properties. *J. Chem. Soc. Faraday Trans. 2* **75**, 38–54 (1979).
45. Liu, A. J. & Nagel, S. R. Nonlinear dynamics: jamming is not just cool any more. *Nature* **396**, 21–22 (1998).
46. Trappe, V., Prasad, V., Cipelletti, L., Segre, P. N. & Weitz, D. A. Jamming phase diagram for attractive particles. *Nature* **411**, 772–775 (2001).
47. Ciamarra, M. P., Pastore, R., Nicodemi, M. & Coniglio, A. Jamming phase diagram for frictional particles. *Phys. Rev. E* **84**, 041308 (2011).
48. Makse, H. A., Johnson, D. L. & Schwartz, L. M. Packing of compressible granular materials. *Phys. Rev. Lett.* **84**, 4160–4163 (2000).
49. Coniglio, A., de Candia, A., Fierro, A., Nicodemi, M. & Tarzia, M. Statistical mechanics approach to the jamming transition in granular materials. *Physica A* **344**, 431–439 (2004).
50. Jaiswal, A., Egami, T., Kelton, K. F., Schweizer, K. S. & Zhang, Y. Correlation between fragility and the Arrhenius crossover phenomenon in metallic, molecular, and network liquids. *Phys. Rev. Lett.* **117**, 205701 (2016).
51. Wu, B., Iwashita, T. & Egami, T. Atomic dynamics in simple liquid: de Gennes narrowing revisited. *Phys. Rev. Lett.* **120**, 135502 (2018).
52. Bi, D., Zhang, J., Chakraborty, B. & Behringer, R. P. Jamming by shear. *Nature* **480**, 355–358 (2011).
53. Hedges, L. O., Jack, R. L., Garrahan, J. P. & Chandler, D. Dynamic order-disorder in atomistic models of structural glass formers. *Science* **323**, 1309–1313 (2009).
54. Li, M.-X. et al. High-temperature bulk metallic glasses developed by combinatorial methods. *Nature* **569**, 99–103 (2019).
55. Lakeland, D. L., Rechenmacher, A. & Ghanem, R. Towards a complete model of soil liquefaction: the importance of fluid flow and grain motion. *Proc. R. Soc. A* **470**, 20130453 (2014).

Methods

Sample preparation. $Zr_{55}Cu_{30}Al_{10}Ni_5$ (at.%) MG is selected as a model system for the broadband stress relaxation experiments. Glassy films with 5 μm thickness were prepared by a single-target magnetron sputtering method using a multicomponent $Zr_{55}Cu_{30}Al_{10}Ni_5$ alloy as the target[56]. The deposition was conducted with a radio frequency power of 100 W at room temperature. The base pressure was 3×10^{-4} Pa, and the working pressure was tuned to 0.3 Pa with high-purity argon gas. Si(100) wafers with a diameter of 50 mm were used as substrates. Free-standing film samples were obtained by dissolving the silicon substrate in NaOH–water solution. The glass transition temperature of the film was measured to be 695 K by differential scanning calorimetry with a PerkinElmer 8500 instrument under a purified argon atmosphere at a heating rate of 20 K min^{-1}, consistent with that of the $Zr_{55}Cu_{30}Al_{10}Ni_5$ bulk samples and previous reports[56,57]. The 5-μm-thick, 25-μm-wide and 200-μm-long cantilevers were machined by focused ion beam in a dual-beam scanning electron microscopy system (FEI Versa 3D) with 30 kV accelerating voltage and 0.5 nA Ga^+ ion current. Larger cantilevers of 30 μm thick, 70 μm wide and 700 μm long were prepared by machining $Zr_{55}Cu_{30}Al_{10}Ni_5$ ribbons using a low-speed saw. Ribbon samples were produced by melt-spinning the $Zr_{55}Cu_{30}Al_{10}Ni_5$ alloy on a copper wheel at a rotation speed of about 420 rad s^{-1} in an argon atmosphere.

Structural characterization. The microstructure of the as-prepared thin films was characterized by transmission electron microscopy (TEM). The TEM samples were prepared by ion milling using a Gatan PIPS-II ion miller equipped with a liquid nitrogen cooling holder. TEM experiments were conducted by a JEOL ARM200F TEM instrument operating at an acceleration voltage of 200 kV. The selected area electron diffraction pattern of the $Zr_{55}Cu_{30}Al_{10}Ni_5$ thin films shows diffusive amorphous halos (Supplementary Fig. 4a), demonstrating the amorphous nature of the samples. The high-resolution TEM image in Supplementary Fig. 4b further verifies that visible crystallites could not be found and that the alloy used in the stress relaxation experiments had a fully amorphous structure. The morphology and size of the cantilever samples and the indents of the nanoindentation experiments were inspected by scanning electron microscopy in a FEI Versa 3D scanning electron microscope with 5 kV accelerating voltage.

Broadband nanoindentation relaxation experiments. The elastic modulus (E) and hardness (H) of the MG were determined to be 121.5 GPa and 6.7 GPa at room temperature (295 K), following the Oliver–Pharr method[58], by a nanoindentation instrument (Hysitron Triboindenter) equipped with a Berkovich indenter at the peak force of 10 mN and loading–unloading rate of 0.2 mN s^{-1}. The nanoindentation relaxation tests were performed by applying the load to 10 mN in 0.05 seconds; holding at 10 mN for up to 200 seconds for quasi-static relaxation measurements and up to 2,000 seconds for dynamic relaxation measurements; and then unloading in 0.05 seconds. Indentation depths were all within 300 nm, much smaller than 10% of the film thickness, avoiding possible influence from substrates. The load and depth were recorded at a data acquisition rate of up to 2,000 points per second for relaxation tests.

In order to obtain reliable and accurate relaxation data, the following procedures were followed. The area function of the probe was carefully calibrated on fused quartz to get area function constants C_1 to C_6 as listed in Supplementary Table 3, using equation (S1)[58]:

$$A(h) = \sum_{i=1}^{6} C_i \cdot (h - 0.75\,P_{\max}/S)^{4/2^i} \tag{S1}$$

where $A(h)$ is the contact area as a function of indentation depth (h), P_{max} is the peak force and S is the contact stiffness measured from unloading segments. The nanoindentation relaxation results in this study were obtained at depths larger than 200 nm to avoid the tip radius effect, which is evident at depths lower than 30 nm. The geometry of the indents for 2,000 s relaxation tests is also characterized by scanning electron microscopy and is shown in Fig. 1b.

In order to minimize the thermal drift effect from the nanoindentation relaxation measurements, all tests were performed at least 2 hours after samples were placed in the instrument chamber for sufficient system stabilization. The typical thermal drift rate of the system was calibrated by a fused quartz sample with 1 μN contact force at every 40 seconds and was plotted in Supplementary Fig. 5a. The thermal drift rates are all within ±0.02 nm s^{-1} in this study. Before each test, the probe was engaged onto the sample surface and there was a wait of 300 seconds for the stage motor and piezo to settle. After that, the thermal drift was monitored for 100 seconds with 1 μN contact force before each test and with 5% peak force after each test. The average thermal drift rate was calculated and subtracted from each relaxation measurement. Typical quasi-static nanoindentation relaxation data with a constant 10 mN force are plotted in Supplementary Fig. 5b. The measured strain rates are all above the thermal drift rate during the 200 s relaxation. Thus, the standard quasi-static nanoindentation relaxation measurement is reliable for as long as 200 seconds, beyond which the thermal drift may interfere with the low-rate measurements. Additional indentation relaxation at lower stress and lower strain rate was measured by loading to 10 mN and then monitoring the dynamic contact stiffness with 0.2 mN load amplitude and 200 Hz frequency for as long as 2,000 seconds. The indentation depth was estimated from the measured dynamic contact stiffness, which had a negligible thermal drift effect because the high dynamic loading frequency was comparable to the low drift rate. The measured contact stiffness (S) was used to estimate the indentation depths (h) following equation (S2)[58]:

$$E = \frac{S\sqrt{\pi}}{2\sqrt{A(h)}} \tag{S2}$$

where E is the Young's modulus (121.5 GPa) and $A(h)$ is the area function equation (S1), both of which are assumed to be constant during the test. Since the displacement amplitude is around 1 nm within a period of 1/200 s, the dynamic displacement rate is above 200 nm s^{-1}, which is much higher than the thermal drift rate of 0.02 nm s^{-1}. Thus, the thermal drift can be ignored, and the measured contact stiffness and calculated indentation depth by equations (S1) and (S2) are plotted as a function of relaxation time in Supplementary Fig. 5c,d respectively. Dynamic tests cannot measure the highest stress and/or strain rate region at the early stage of relaxation, for example 0–20 s; therefore, the static (0–200 s, Supplementary Fig. 5b) and dynamic (20–2,000 s, Supplementary Fig. 5d) relaxation results are plotted together in Supplementary Fig. 5e, and they overlap well in the time range from 20 s to 200 s and form a continuous line.

With the nanoindentation measurements, the shear strain rate ($\dot{\gamma}$) beneath the indenter is derived from the displacement rate (dh/dt) and depth (h) through the following equation[59]:

$$\dot{\gamma} = 0.16\frac{1}{h}\frac{dh}{dt} \tag{S3}$$

The hardness of the $Zr_{55}Cu_{30}Al_{10}Ni_5$ MG was measured to be 6.7 GPa at room temperature, which is about 3.5 times the compression strength of 1.9 GPa (ref. [57]). Since the pure shear stress is approximately $\sqrt{3}$ times lower than the uniaxial yield stress under the monotonic loading conditions according to the von Mises yield criterion, the hardness/shear-strength ratio is approximately $3.5\sqrt{3}$. Thus, the nominal shear stress (τ) can be estimated from indentation depth (h) and load (P) by the following:

$$\tau = \frac{\sigma}{\sqrt{3}} = \frac{P}{3.5\sqrt{3}A(h)} \tag{S4}$$

where σ is the normal stress and $A(h)$ is the area function of the indenter, which was carefully calibrated before and after the relaxation tests. With the data of depth versus time in Supplementary Fig. 5e at a constant force of 10 mN, the nominal shear stress and shear strain rate as a function of time can be derived and are plotted in Supplementary Fig. 5f. The nominal shear stress beneath the indenter decreases from 1,402.6 ± 5 MPa to 1,057.1 ± 35 MPa during the relaxation from 0 s to 2,000 s. Accordingly, the strain rate in relaxation testing covers more than four orders of magnitude from 0.56 s^{-1} to 5.3×10^{-6} s^{-1} (Supplementary Fig. 5f). The estimated shear stress is plotted as the function of the shear strain rate in Fig. 1b, in which the shear stress has a linear log–log relation with the shear strain rate in the high-stress region above 1,350 MPa. The slope of the linear portion, or the strain-rate sensitivity ($m = \partial \ln \tau/\partial \ln \dot{\gamma}$), is calculated to be 0.004 ± 0.001, consistent with that of the rate-jump indentation measurements[17]. The strain-rate sensitivity gradually increases to ~0.5 when the strain rate decreases to ~3×10^{-5} s^{-1} and the stress is below 1,100 MPa. For the broadband nanoindentation experiments, the strain rate approaches the limit when the relaxation extends for longer than 2,000 s, with a resulting strain rate of 5.3×10^{-6} s^{-1}. Beyond the time limit, the relaxation measurements will be obviously interfered with by lateral thermal drift. To overcome the technical limitation, we employed a nanoindenation-based cantilever bending method[60] to detect the flow behaviour of MGs in a low-strain-rate range from 10^{-8} to 10^{-6} s^{-1}.

Cantilever relaxation experiments. Typical cantilevers with sizes are shown in Supplementary Fig. 6a,b. A conical indenter with 1.5 μm tip radius was loaded on the cantilever with a constant force of 1.0, 1.5, 2, 2.5, 3, 3.5, 4.5, 6, 8 and 10 mN using a Hysitron Triboindenter. The distance between the clamp and indenter tip contact point was 400 μm for $30\times70\times700$ μm^3 cantilevers and 50 μm for $5\times25\times200$ μm^3 cantilevers. The indenter displacement was measured during the constant force relaxation for 1,000 seconds, and anelastic recovery was also monitored for 1,000 seconds with 1 μN force. Thermal drift was measured with 1 μN contact force for 200 seconds before each test and was subtracted. Indenter displacements, or cantilever deflection displacements (h'), as a function of time during relaxation tests are plotted in Supplementary Fig. 6c,d for 5-μm-thick and 30-μm-thick cantilevers, respectively. The corresponding shear stresses (τ) and instantaneous shear strains (γ_i) at the pivot point of the cantilevers are calculated by

$$\tau = \frac{6PL}{\sqrt{3}wb^2} \text{ and } \gamma_i = \frac{3\sqrt{3}bh'}{2L^2}, \tag{S5}$$

where P is the load, L is the distance between the clamp and indenter tip contact point, b is the sample thickness, w is the width of the cantilever and h' is the

bending displacement[60]. Calculated shear strains at the pivot point under constant loading forces of 1 to 10 mN in the cantilevers are plotted as a function of time in Supplementary Fig. 6c,d. The instantaneous shear strain rate at the pivot point as shown in Fig. 1a, therefore, can be derived by taking the time derivative of the instantaneous shear strain equation (S5). The relaxation process is readily observed in the constant force segment and anelastic recovery takes place in the unloading segment. The permanent strain is obtained by subtracting the anelastic strain (γ_a) from the total relaxation strain (γ_t) to estimate plastic shear strain rates, $\dot{\gamma} = (\gamma_t - \gamma_a)/\Delta t$, at various stresses for a duration of $\Delta t = 1{,}000$ s and are plotted with shear stress in Fig. 1c. The measured strain rates cover the range from 10^{-8} to $10^{-6}\,s^{-1}$. The strain rate sensitivity (m) keeps increasing with the decrease of strain rate and reaches a constant value of ~1.0 when the strain rate is lower than $10^{-7}\,s^{-1}$ in Fig. 1c.

Data availability

The authors declare that the data supporting the findings of this study are included within the paper and its Supplementary Information file. Source data are provided with this paper.

References

56. Liu, Y. H. et al. Deposition of multicomponent metallic glass films by single-target magnetron sputtering. *Intermetallics* **21**, 105–114 (2012).
57. Yang, R. Q., Fan, J. T., Li, S. X. & Zhang, Z. F. Fracture behavior of $Zr_{55}Cu_{30}Al_{10}Ni_5$ bulk metallic glass under quasi-static and dynamic compression. *J. Mater. Res.* **23**, 1744–1750 (2008).
58. Oliver, W. C. & Pharr, G. M. An improved technique for determining hardness and elastic-modulus using load and displacement sensing indentation experiments. *J. Mater. Res.* **7**, 1564–1583 (1992).
59. Poisl, W. H., Oliver, W. C. & Fabes, B. D. The relationship between indentation and uniaxial creep in amorphous selenium. *J. Mater. Res.* **10**, 2024–2032 (1995).
60. Weihs, T. P., Hong, S., Bravman, J. C. & Nix, W. D. Mechanical deflection of cantilever microbeams: a new technique for testing the mechanical properties of thin films. *J. Mater. Res.* **3**, 931–942 (1988).

Acknowledgements

S.S. is supported by the National Natural Science Foundation of China (grant no. 51821001) and MOST 973 of China (grant no. 2015CB856800). M.C. is supported by the National Science Foundation (NSF DMR-1804320) with J. Yang as the programme director. F.Z. is sponsored by the Shanghai Pujiang Program under grant no. 21PJ1401800. We also thank the staff from the Shanghai Key Laboratory of Advanced High-Temperature Materials and Precision Forming for assistance during data collection.

Author contributions

S.S. designed and performed the broadband stress relaxation experiments and data processing; F.Z. prepared the MG samples and conducted the microstructure characterization; and S.S. and M.C. analysed the data, developed the models and wrote the paper. M.C. conceived and supervised the project.

Competing interests

The authors declare no competing interests.

Additional information

Supplementary information The online version contains supplementary material available at https://doi.org/10.1038/s41563-021-01185-y.

Correspondence and requests for materials should be addressed to Mingwei Chen.

Peer review information *Nature Materials* thanks Jean Marc Pelletier and the other, anonymous, reviewer(s) for their contribution to the peer review of this work.

Reprints and permissions information is available at www.nature.com/reprints.